Structures of Larger Proteins in Solution: Three- and Four-Dimensional Heteronuclear NMR Spectroscopy

G. MARIUS CLORE AND ANGELA M. GRONENBORN

Three- and four-dimensional heteronuclear nuclear magnetic resonance (NMR) spectroscopy offers dramatic improvements in spectral resolution by spreading through-bond and through-space correlations in three and four orthogonal frequency axes. Simultaneously, large heteronuclear couplings are exploited to circumvent problems due to the larger linewidths that are associated with increasing molecular weight. These novel experiments have been designed to extend the application of NMR as a method for determining three-dimensional structures of proteins in solution beyond the limits of conventional two-dimensional NMR (~100 residues) to molecules in the 150- to 300-residue range. This potential has recently been confirmed with the determination of the high-resolution NMR structure of a protein greater than 150 residues, namely, interleukin-1β.

A COMPLETE UNDERSTANDING OF PROTEIN FUNCTION AND mechanism of action can only be accomplished with a knowledge of its three-dimensional (3D) structure at atomic resolution. At the present time there are two methods available for determining such structures. The first method, which has been established for many years, is x-ray diffraction of protein single crystals. The second method has only blossomed in the last 5 years and is based on the application of nuclear magnetic resonance (NMR) spectroscopy (*1*) of proteins in solution. The driving force for the development of an alternative to x-ray crystallography was threefold. First, many proteins do not crystallize, and even when they do the crystals may diffract poorly or there may be difficulties in solving the phase problem (such as finding suitable heavy-atom derivatives). Second, significant and possibly important functional differences may exist between structures in the crystal state and in solution. Third, dynamic processes ranging from the picosecond to second time scales are amenable to study by NMR. Despite these attractive features, it should be borne in mind that, just like crystallography, NMR also has a number of limitations. In particular, the protein under investigation must be soluble and should not aggregate up to a concentration of at least 1 mM. Further, the dependence of linewidth on rotational correlation time probably sets an intrinsic upper molecular weight limit of about 50 to 60 kD for the applicability of current solution NMR technology.

The advent of 2D NMR (*2, 3*) set the stage for the determination of the first low-resolution structures of small proteins in the mid-1980s (*4–7*). Subsequent improvements during the next few years led to a tremendous increase in the precision and accuracy of such protein structure determinations that it is now possible, with the use of 2D NMR methods, to determine structures of proteins up to ~100 residues that are comparable in quality to 2 to 2.5 Å resolution x-ray structures. This progress has been summarized in a number of reviews (*8, 9*). For proteins larger than ~100 residues, however, conventional 2D methods can no longer be applied successfully. This review focuses on the novel methodological developments of heteronuclear 3D and 4D NMR, which have been designed to overcome the limitations imposed by the increased molecular weight and spectral complexity inherent to these proteins, and describes their application, which has recently culminated in the determination of high-resolution NMR structure of a protein greater than 150 residues (*10*).

The concept of increasing spectral dimensionality to extract information can perhaps most easily be understood by analogy. Consider for example an encyclopedia. In a 1D representation, all of the information (that is, words and sentences arranged in a particular set order) present in the encyclopedia would be condensed into a single line. If this line were expanded to two dimensions in the form of a page, the odd word may be resolved but the vast majority would still be superimposed on each other. When this page is expanded into a book (that is, three dimensions) comprising a set number of lines and words per page, as well as a fixed number of pages, some pages may become intelligible, but many words would still lie on top of each other. The final expansion to the multivolume book (that is, four dimensions) then makes it possible to extract in full all of the information present in the individual entries of the encyclopedia.

Structural Data from NMR Measurements

The principal source of geometric information used in NMR protein structure determination lies in short approximate interproton distance restraints (r) derived from nuclear Overhauser enhancement (NOE) measurements (*11*). The physical basis for the NOE effect is relatively simple and is based on the fact that each proton spin possesses a property known as magnetization. Magnetization is exchanged between the spins by a process termed cross relaxation, and the rate constant for this process is directly related to r^{-6}. The

The authors are in the Laboratory of Chemical Physics, Building 2, National Institute of Diabetes and Digestive and Kidney Diseases, National Institutes of Health, Bethesda, MD 20892.

chemical analogy to such a system is one with a large number of interconverting species in equilibrium with each other. Cross relaxation can be measured by perturbing the magnetization of a particular spin and observing the resulting change in magnetization (the NOE) of the other spins as the equilibrium is reestablished. Thus, the time dependence of the NOE is governed by a set of coupled first-order differential equations. The experiment is therefore similar to chemical relaxation kinetics (such as a temperature jump experiment), except that the initial perturbation in the chemical system involves rate constants rather than species concentration. If the NOE is observed only a short time after the perturbation, the size of the NOE is proportional to the cross-relaxation rate and hence to r^{-6}. Because of the r^{-6} dependence, the magnitude of these effects decreases rapidly as the interproton distances increase, so that NOEs are generally not observable beyond 5 Å. The interproton distance restraints derived from the NOE measurements may also be supplemented by backbone and side chain torsion angle restraints derived from three-bond coupling constants and appropriate NOEs (*12–15*).

With the approximate interproton distance and torsion angle restraints in hand, a number of computational strategies can be applied to locate the minimum of a target function comprising terms for the experimental restraints, covalent geometry (that is, bonds, angles, planes, and chirality), and nonbonded contacts (such as a van der Waals repulsion term to prevent atoms from coming too close together). The types of algorithms used operate either in *n*-dimensional distance space followed by projection into real space [such as metric matrix distance geometry (*16*)] or directly in real space [such as minimization in torsion angle space with a variable target function (*17*), dynamical simulated annealing (*18, 19*), and restrained molecular dynamics (*5–7, 20*)]. All of the real space methods require initial structures, which can be random structures with correct covalent geometry, structures very far from the final structure (such as extended strand), structures made up of a completely random array of atoms, or structures generated by distance space methods. The key requirements of all of these methods is that they have large radii of convergence and that they fully sample in an unbiased fashion the conformational space consistent with the experimental, geometrical, and van de Waals restraints (*9*). The various methods have been described in detail in a number of reviews (*9, 21*) and have all been successfully applied to NMR structure determinations.

In order to assess the accuracy and precision of an NMR structure determination, it is essential to calculate a large number of structures independently with the same experimental data set by using different starting structures or conditions. The spread of structures consistent with the experimental data can be assessed qualitatively from a visual inspection of a best fit superposition of a series of computed conformers and quantitatively by calculating the average atomic root-mean-square (rms) distribution of the individual structures about the mean coordinate positions. The representation of NMR solution structures as an ensemble of conformers in which each individual member is compatible with the experimental data may still be regarded as unusual, insofar that one has long been accustomed to the traditional single chain trace representation of x-ray structures. In the latter case, a single polypeptide chain is usually fitted to the electron density map, although one has to bear in mind that the density arises from a linear superposition of all of the different conformers present within the crystal.

The power of the NMR method and an illustration of the progressive improvement in NMR protein structures as a function of increasing only the number, rather than the precision, of experimental restraints is shown in Fig. 1. Thus, in all of the examples shown in Fig. 1, the NOE-derived interproton distance restraints

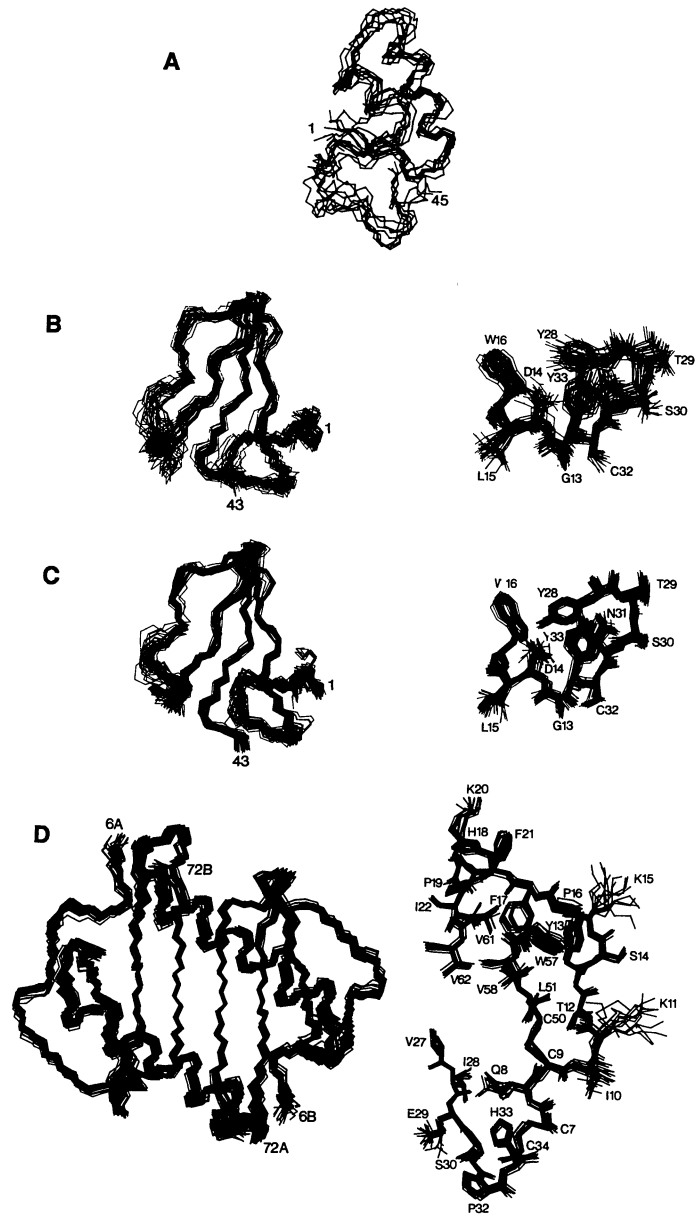

Fig. 1. Illustration of the progressive improvement in the precision and accuracy of NMR structure determinations with increasing number of experimental restraints. (**A**) First-generation structure: ~7 restraints per residue; rmsd = 1.5 Å for backbone atoms, 2.0 Å for all atoms; example, α1-purothionin. (**B**) Second-generation structure: ~10 restraints per residue; rmsd = 0.9 Å for backbone atoms, 1.2 Å for all atoms; example, BDS-I. (**C**) Third-generation structure: ~13 restraints per residue, rmsd = 0.7 Å for backbone atoms, 0.9 Å for all atoms; example, BDS-I. (**D**) Fourth-generation structure: ~16 restraints per residue; rmsd = 0.4 Å for backbone atoms, 0.9 Å for all atoms, ≤0.5 Å for ordered side chains; example, interleukin-8. The fourth-generation structures are equivalent in quality to ~2 to 2.5 Å resolution x-ray structures. Each protein is represented by a best fit superposition of a number of independently computed conformers: there are 9 for α1-purothionin, 31 for the second-generation version of BDS-1, 42 for the third-generation of BDS-1, 30 for the backbone atoms of interleukin-8, and 15 for the side chains of interleukin-8. In all of the examples shown, the NOE-derived interproton distance restraints are only classified into three broad ranges, 1.8 to 2.7 Å, 1.8 to 3.3 Å, and 1.8 to 5.0 Å, which correspond to strong, medium, and weak NOEs, respectively. The structure of α1-purothionin (7) was calculated by metric matrix distance geometry (*16*) followed by restrained molecular dynamics (*20*), whereas the structures of BDS-I (*22, 23*) and interleukin-8 (*24*) were calculated by using the hybrid distance geometry-simulated annealing method (*18*). The rmsd is the average atomic rms distribution of the individual calculated structures about the mean coordinate positions.

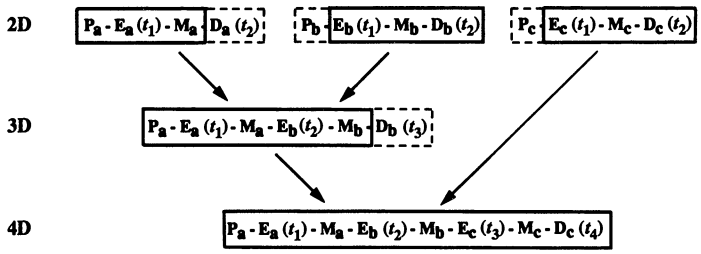

Fig. 2. General representation of pulse sequences used in multidimensional NMR illustrating the relation between the basic schemes used to record 2D, 3D, and 4D NMR spectra. Note how 3D and 4D experiments are constructed by the appropriate linear combination of 2D ones. Abbreviations: P, preparation; E, evolution; M, mixing; and D, detection. In 3D and 4D NMR, the evolution periods are incremented independently.

are only approximate and classified into three broad ranges, 1.8 to 2.7 Å, 1.8 to 3.3 Å, and 1.8 to 5.0 Å, which correspond to strong, medium, and weak NOEs, respectively. First-generation structures, such as α1-purothionin (45 residues) (*7*), were based on five to seven experimental restraints per residue. The atomic rms distribution of the backbone atoms is rather large (~1.5 Å) so that while a cartoon-like representation of the polypeptide fold is obtained, details of both the local backbone and side chains conformations are essentially obscured by the large variations between the structures. As the experimental restraints are increased to about ten per residue, including some backbone ϕ torsion angle restraints derived from a qualitative interpretation of the $^3J_{HN\alpha}$ couplings, a significant improvement is observed and the resulting second-generation structures have a backbone atomic rms distribution of ~0.9 Å (*22*). The side chain conformations, however, are still rather blurred. Additional improvement requires stereospecific assignments of β-methylene protons and χ_1 side chain torsion angle restraints. In a simplified approach these data are obtained from a qualitative interpretation of $^3J_{\alpha\beta}$ coupling constants and intraresidue NOEs (*12*). The resulting third-generation structures are based on ~13 experimental restraints per residue and display a marked improvement not only in the definition of the backbone atoms, but more importantly in the side chains as well (*23*), which is readily apparent by comparing the second- (*22*) and third-generation (*23*) structures of the same protein, BDS-I (43 residues). Finally, in the fourth-generation structures, a much larger number of stereospecific assignments and loose torsion angle restraints are obtained by carrying out conformational grid searches of ϕ,ψ,χ_1 torsion angle space on the basis of the $^3J_{HN\alpha}$ and $^3J_{\alpha\beta}$ coupling constants and intraresidue and sequential interresidue NOEs involving the NH, CαH, and CβH protons (*12, 14*). This approach leads to 16 to 20 experimental restraints per residue, a backbone atomic rms distribution of ≤0.4 Å, and an atomic rms distribution of ≤0.5 Å for ordered side chains. The errors in the atomic coordinates of such fourth-generation structures, like that of interleukin-8 (a dimer with 72 residues per subunit) (*24*) shown in Fig. 1, are similar to those of 2 to 2.5 Å resolution x-ray structures (*25*). Indeed, the solution structure of interleukin-8 was used by necessity to solve the x-ray structure by molecular replacement, as traditional methods based on heavy atom derivatives had proved unsuccessful, despite several years of effort (*26*).

Although many examples of first- and second-generation structures have been reported, relatively few third- and fourth-generation structures have been reported. In addition to the two structures shown in Fig. 1, examples of third-generation structures are tendamistat (*27*), hirudin (*28*), and *Escherichia coli* thioredoxin (*29*), whereas examples of fourth-generation structures are the COOH-terminal domain of cellobiohydrolase (*14*), the homeodomain of the *Antennapedia* protein (*30*), a zinc finger domain from a human enhancer binding protein (*31*), human thioredoxin (*32*), and interleukin-1β (IL-1β) (*10*).

Deriving Experimental Restraints from NMR Data

The experimental restraints derived from the NMR data require the identification of specific interactions between proton pairs, which may be either through-space (through the NOE) or through-bonds (through coupling constants). The power of the NMR method compared to other spectroscopic techniques lies in the fact that each proton gives rise to a specific resonance in the spectrum. Thus, a key aspect of any NMR structure determination is the requirement to assign each resonance to an individual proton and then to uniquely identify each pairwise through-space NOE interaction. In principle this can be accomplished in a relatively straightforward manner by using correlation experiments to identify resonances belonging to different amino acid types via through-bond connectivities and NOE experiments to subsequently link these residues in a sequential manner along the polypeptide chain on the basis of sequential and short-range interresidue NOEs involving the NH, CαH, and CβH protons (*8, 9*). In particular, the types of NOE interactions that are most instructive for this purpose involve NH(i)-NH(i+1,2), CαH(i)-NH(i+1,2,3,4), CβH(i)-NH(i+1), and CαH(i)-CβH(i+3) connectivities, and the pattern of observed NOEs provides a very good indication of the different secondary structure elements along the polypeptide chain. With the resonance assignments in hand, one can then proceed to identify long-range NOE interactions between protons belonging to residues far apart in the sequence but close together in space, a process that yields crucial information for determining the tertiary structure of the protein.

While the principles of sequential resonance assignment are simple, the practice is difficult. Even for a small protein of about 50 residues, there are likely to be some 300 to 400 protons for which resonances have to be uniquely assigned. This number goes up linearly with the number of residues, so that for a 150-residue protein there will be 900 to 1200 protons. Because of the large number of protons, there is an extensive degree of resonance overlap and chemical shift degeneracy. As a result, 1D NOE and decoupling experiments can only be applied with any degree of confidence for peptides up to about ten residues, and even then there may be serious difficulties. The major conceptual advance in the application of NMR as a method of protein structure determination was the introduction of 2D NMR (*2, 3*). By spreading out the correlations in two ^1H frequency dimensions, each interaction is labeled by two chemical shifts, namely, the frequencies of the originating and destination protons. This approach not only results in a tremendous increase in spectral resolution but equally importantly it enables one to detect and interpret effects that would not have been possible in one dimension.

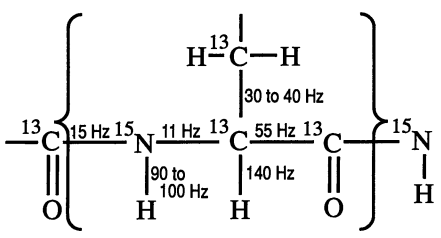

Fig. 3. Summary of the one-bond heteronuclear couplings along the polypeptide chain used in 3D and 4D NMR experiments. The backbone torsion angles ϕ and ψ involve rotations about the N_i–$C\alpha_i$ and $C\alpha_i$–C_i bonds, respectively, whereas the side chain torsion angle χ_1 involves a rotation about the $C\alpha_i$–$C\beta_i$ bond.

All 2D experiments can be reduced to the same basic conceptual scheme shown in Fig. 2 (*3*). This comprises a preparation pulse, an evolution period (t_1) during which the spins are labeled according to their chemical shifts, a mixing period (M_1) during which the spins are correlated with one another, and finally a detection period (t_2). The experiment is repeated several times with successively linearly incremented values of the evolution period t_1 to yield a data matrix $s(t_1,t_2)$. Fourier transformation in the t_2 dimension yields a set of n 1D spectra in which the intensities of the resonances are sinusoidally modulated as a function of the t_1 duration. Subsequent Fourier transformation in the t_1 dimension yields the desired 2D spectrum $S(\omega_1,\omega_2)$.

Such 2D methods have proved extremely powerful for the structure determination of small proteins. The largest proteins (in terms of number of residues) where this approach has been successfully applied to achieve a complete 3D structure determination are *E. coli* (*29*) and human thioredoxin (*32*), which have 108 and 105 residues, respectively. Beyond this limit of ~100 residues, 2D methods soon break down because of two fundamental problems. The first is associated with extensive spectral overlap due to the larger number of resonances. Consequently, the contour plot of a 2D spectrum of a 150-residue protein assumes the appearance of an intangible network of intersecting circles as an ever larger number of cross peaks merge into one another. The result is that the 2D spectra of such a protein can no longer be interpreted. The second is a sharp decrease in the efficiency with which magnetization can be transferred through the small three-bond ^1H-^1H J couplings (3 to 12 Hz) as the linewidths become larger than the couplings because of the increasing rotational correlation time. This effect leads to incomplete delineation of spin systems (that is, amino acid types) in through-bond correlation experiments.

Solutions to both these problems are obtained by extending the dimensionality of the NMR spectra to remove resonance overlap and degeneracy and by making use of through-bond correlations via heteronuclear couplings that are larger than the linewidths. This method necessitates the use of proteins uniformly labeled with ^{15}N, ^{13}C, or both. In proteins that can be overexpressed in bacterial systems, such labeling can be readily achieved by growing the organism in minimal medium supplemented by $^{15}NH_4Cl$ or [$^{13}C_6$]glucose (or both) as the sole nitrogen and carbon sources, respectively.

Basics of 3D and 4D NMR

The design and implementation of higher dimensionality NMR experiments can be carried out by the appropriate combination of 2D NMR experiments (Fig. 2) (*33, 34*). A 3D experiment is constructed from two 2D pulse schemes by leaving out the detection period of the first experiment and the preparation pulse of the second. This results in a pulse train comprising two independently incremented evolution periods t_1 and t_2, two corresponding mixing periods M_1 and M_2, and a detection period t_3. Similarly, a 4D experiment is obtained by combining three 2D experiments in an analogous fashion. Thus, conceptually n-dimensional NMR can be conceived as a straightforward extension of 2D NMR. The real challenge, however, of 3D and 4D NMR is twofold: first, to ascertain which 2D experiments should be combined to best advantage; and second, to design the pulse sequences in such a way that undesired artifacts, which may severely interfere with the interpretation of the spectra, are removed. This task is far from trivial.

The first application of 3D NMR to a small protein, namely α1-purothionin, was presented in 1988 (*34*). The experiment was of the proton homonuclear variety in which a through-bond correlation experiment (HOHAHA) was combined with a through-space one (NOESY). Although this experiment demonstrated the potential of the methodology, it suffered from a number of drawbacks that severely limited its application to larger proteins. First, the correlation portion of the experiment relied on small ^1H-^1H couplings. Second, all homonuclear 3D spectra are substantially more difficult to interpret than the equivalent 2D versions, as the number of cross peaks present in the former far exceeds that in the latter.

Fortunately, heteronuclear 3D and 4D NMR experiments do not suffer from any of these disadvantages and yield important additional information in the form of ^{15}N and ^{13}C chemical shifts (*35–48*). They exploit a series of large one-bond heteronuclear couplings for magnetization transfer through-bonds, as summarized in Fig. 3. This, together with the fact that the ^1H nucleus is always detected, renders these experiments very sensitive. Indeed, high-quality 3D and 4D heteronuclear-edited spectra can easily be obtained on samples of 1 to 2 mM uniformly labeled protein in a time frame that is limited solely by the number of increments that have to be collected for appropriate digitization and the number of phase-cycling steps that have to be used to reduce artifacts to an acceptably low level. Typical measurement times are 1.5 to 3 days for 3D experiments and 2.5 to 5 days for 4D ones.

Many of the 3D and 4D experiments are based on heteronuclear-

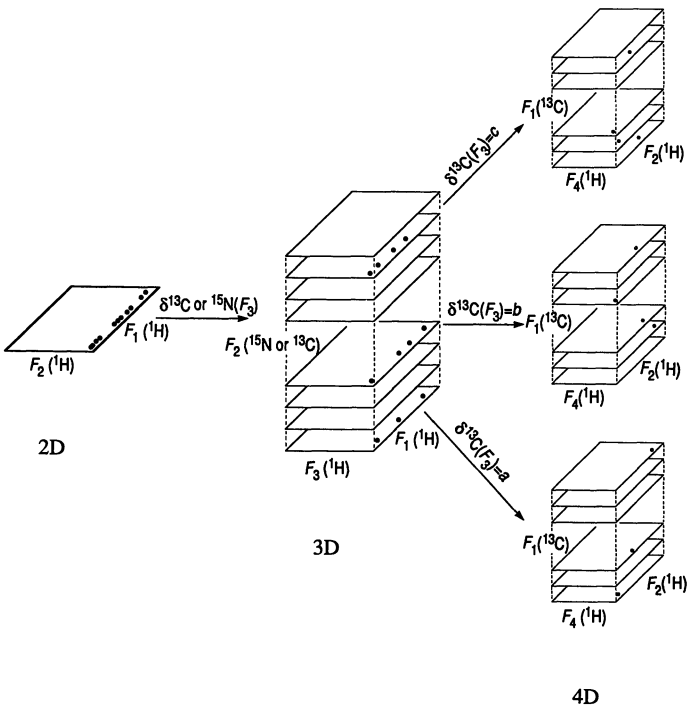

Fig. 4. Schematic illustration of the progression and relation between 2D, 3D, and 4D heteronuclear NMR experiments. The closed circles represent NOE cross peaks. In the example shown there are 11 NOEs originating from 11 different protons in the F_1 dimension to a single frequency position in the F_2 dimension. In the 2D spectrum, it is impossible to ascertain whether there is only one destination proton or several in the F_2 dimension. By spreading the spectrum into a third dimension (labeled F_2) according to the chemical shift of the heteronucleus attached to the destination proton, it can be seen that the NOEs now lie in three distinct $^1H(F_1)$-$^1H(F_3)$ planes, indicating that three different destination protons are involved. However, the ^1H chemical shifts still provide the only means of identifying the originating protons. Hence the problem of spectral overlap still prevents the unambiguous assignment of these NOEs. By extending the dimensionality of the spectrum to four, each NOE interaction is labeled by four chemical shifts along four orthogonal axes. Thus, the NOEs in each plane of the 3D spectrum are now spread over a cube in the 4D spectrum according to the chemical shift of the heteronucleus directly attached to the originating protons. Adapted from (*44*).

editing of ^1H-^1H experiments so that the general appearance of conventional 2D experiments is preserved and the total number of cross peaks present is the same as that in the 2D equivalents (*35–46*). The progression from a 2D spectrum to 3D and 4D heteronuclear-edited spectra is depicted schematically in Fig. 4. Consider, for example the cross peaks involving a particular ^1H frequency in a 2D NOESY spectrum, a 3D ^{15}N- or ^{13}C-edited NOESY spectrum, and finally a 4D ^{15}N-^{13}C– or ^{13}C-^{13}C–edited NOESY spectrum. In the 2D spectrum, a series of cross peaks are seen from the originating proton frequencies in the F_1 dimension to the single destination ^1H frequency along the F_2 dimension. From the 2D experiment it is impossible to ascertain whether these NOEs involve only a single destination proton or several destination protons with identical chemical shifts. By spreading the spectrum into a third dimension according to the chemical shift of the heteronucleus attached to the destination proton or protons, NOEs involving different destination protons appear in distinct ^1H-^1H planes of the 3D spectrum. Thus each interaction is simultaneously labeled by three chemical shift coordinates along three orthogonal axes of the spectrum. The projection of all of these planes onto a single plane yields the corresponding 2D spectrum. For the purposes of sequential assignment, heteronuclear-edited 3D spectra are often sufficient for analysis. However, when the goal of the analysis is to assign NOEs between protons far apart in the sequence, a 3D ^{15}N- or ^{13}C-edited NOESY spectrum often proves inadequate because the originating protons are only specified by their ^1H chemical shifts and, more often than not, there are several protons that resonate at the same frequencies. For example, in the case of the 153-residue protein IL-1β, there are ~60 protons that resonate in a 0.4-ppm interval between 0.8 and 1.2 ppm (*43*). Such ambiguities can then be resolved by spreading out the 3D spectrum still further into a fourth dimension according to the chemical shift of the heteronucleus attached to the originating protons so that each NOE interaction is simultaneously labeled by four chemical shift coordinates along four orthogonal axes, namely, those of the originating and destinations protons and those of the corresponding heteronuclei directly bonded to these protons (*44–46*). The result is a 4D spectrum in which each plane of the 3D spectrum constitutes a cube in the 4D spectrum.

For illustration purposes it is also useful to compare the type of information that can be extracted from a very simple system with the use of 2D, 3D, and 4D NMR. Consider a molecule with only two NH and two aliphatic protons in which only one NH proton is close to an aliphatic proton. In addition, the chemical shifts of the NH protons are degenerate, as are those of the aliphatic protons, so that only two resonances are seen in the 1D spectrum. In the 2D NOESY spectrum, an NOE would be observed between the resonance position of the NH protons and the resonance position of the aliphatic protons, but it would be impossible to ascertain which one of the four possible NH-aliphatic proton combinations gives rise to the NOE. By spreading the spectrum into a third dimension, for example, by the chemical shift of the ^{15}N atoms attached to the NH protons, the number of possibilities would be reduced to two, provided, of course, that the chemical shifts of the two nitrogen atoms are different. Finally, when the fourth dimension corresponding to the chemical shift of the ^{13}C atoms attached to the aliphatic protons is introduced, a unique assignment of the NH-aliphatic proton pair giving rise to the NOE can be made.

Heteronuclear 3D and 4D NMR in Practice

A portion of the 2D ^{15}N-edited NOESY spectrum of IL-1β is shown in Fig. 5A to illustrate NOE interactions between the NH protons along the F_2 axis and the CαH protons along the F_1 dimension. Although a large number of cross peaks can be resolved, many of the cross peaks have identical chemical shifts in one or other dimensions. For example, there are 15 cross peaks involving NH protons at a $F_2(^1H)$ chemical shift of ~9.2 ppm. A single $^1H(F_1)$-$^1H(F_3)$ plane of the 3D ^{15}N-edited NOESY spectrum of IL-1β at $\delta^{15}N(F_2)$ = 123.7 ppm is shown in Fig. 5B. Not only is the number of cross peaks in this slice small, but at $\delta^1H(F_3) \approx 9.2$ ppm there is only a single cross peak involving one NH proton. The correlations observed in the ^{15}N-edited NOESY spectrum (*35, 36, 38*) are through-space ones. Intraresidue correlations from the NH protons to the CαH and CβH protons can similarly be resolved by using a 3D ^{15}N-edited HOHAHA spectrum (*36, 37*) in which efficient isotropic mixing sequences are used to transfer magnetization between protons through three-bond ^1H-^1H couplings.

The 3D ^{15}N-edited NOESY and HOHAHA spectra constitute only one of several versions of a 3D heteronuclear-edited spectrum. Many alternative through-bond pathways can be used to great effect. Consider, for example, the delineation of amino acid spin systems, which involves grouping those resonances that belong to the same residue. In 2D NMR, correlation experiments are used to delineate

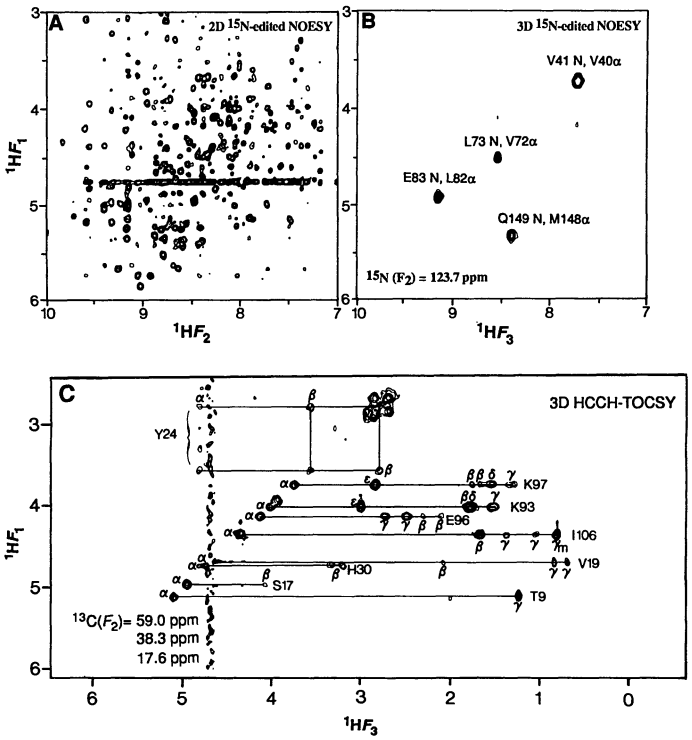

Fig. 5. Example of 2D and 3D spectra of IL-1β recorded at 600 MHz (*38, 43*). The 2D spectrum in (**A**) shows the NH(F_2 axis)-CαH(F_1 axis) region of a 2D ^{15}N-edited NOESY spectrum. The same region of a single NH(F_3)-$^1H(F_1)$ plane of the 3D ^{15}N-edited NOESY at $\delta^{15}N(F_2)$ = 123.7 ppm is shown in (**B**). The actual 3D spectrum comprises 64 such planes and projection of these on a single plane would yield the same spectrum as in (A). In (**C**) a single $^1H(F_3)$-$^1H(F_1)$ plane of the 3D HCCH-TOCSY spectrum at $\delta^{13}C(F_2)$ = 38.3 ± nSW (where SW is the spectral width of 20.71 ppm in the ^{13}C dimension) illustrates both direct and relayed connectivities originating from the CαH protons. It is easy to delineate complete spin systems of long side chains such as Lys (that is, cross peaks to the CβH, CγH, CδH, and CεH protons are observed) because magnetization along the side chain is transferred through large $^1J_{CC}$ couplings. Several features of the HCCH-TOCSY spectrum should be pointed out. First, extensive folding is used that does not obscure analysis as ^{13}C chemical shifts for different carbon types are located in characteristic regions of the ^{13}C spectrum with little overlap (*41–43*). Second, the spectrum is edited according to the chemical shift of the heteronucleus attached to the originating proton rather than the destination one. Third, multiple cross checks on the assignments are readily made by looking for the symmetry-related peaks in the planes corresponding to the ^{13}C chemical shifts of the destination protons in the original slice.

either direct or relayed connectivities through small three-bond ^1H-^1H couplings. Even for proteins of 50 to 60 residues, it can be difficult to delineate long-chain amino acids such as Lys and Arg in this manner. In heteronuclear 3D NMR, an alternative pathway can be used that involves transferring magnetization first from a proton to its directly attached carbon atom through the large $^1J_{CH}$ coupling (~130 Hz), followed by either direct or relayed transfer of magnetization along the carbon chain via the $^1J_{CC}$ couplings (~30 to 40 Hz), before transferring the magnetization back to protons (*41–43, 47*). An example of such a spectrum is the so-called HCCH-TOCSY (*42, 43*) shown in Fig. 5C. The $^1H(F_1)$-$^1H(F_3)$ plane at $\delta^{13}C(F_2)$ = 59 ppm illustrates both direct and relayed connectivities along various side chains originating from CαH protons. As expected, the resolution of the spectrum is excellent and there is no spectral overlap. Just as importantly, however, the sensitivity of the experiment is extremely high and complete spin systems are readily identified in IL-1β even for long side chains, such as those of two Lys residues shown in Fig. 5C. Indeed, analyzing spectra of this kind, it was possible to obtain complete ^1H and ^{13}C assignments for the side chains of IL-1β (*43*).

Experiments can be devised with 3D NMR for sequential assignment that are based solely on through-bond connectivities via heteronuclear couplings (*48*) and which do not rely on the NOESY experiment. This ability becomes increasingly important for studying larger proteins, as the types of connectivities observed in these correlation experiments are entirely predictable, whereas in the NOESY spectrum, which relies solely on close proximity of protons, it may be possible to confuse sequential connectivities with long-range ones. These 3D heteronuclear correlation experiments are of the triple-resonance variety and make use of one-bond $^{13}CO(i-1)$-$^{15}N(i)$, $^{15}N(i)$-$^{13}C\alpha(i)$, and $^{13}C\alpha(i)$-$^{13}CO(i)$ couplings, as well as two-bond $^{13}C\alpha(i-1)$-$^{15}N(i)$ couplings. In this manner multiple independent pathways for linking the resonances of one residue with those of its adjacent neighbor are available, thereby avoiding ambiguities in the sequential assignment.

The power of 4D heteronuclear NMR spectroscopy for unraveling interactions that would not have been possible in lower dimensional spectra is illustrated in Fig. 6 by the ^{13}C-^{13}C–edited NOESY spectrum of IL-1β (*45*). A small portion of the aliphatic region between 1 and 2 ppm of a conventional 2D NOESY spectrum of

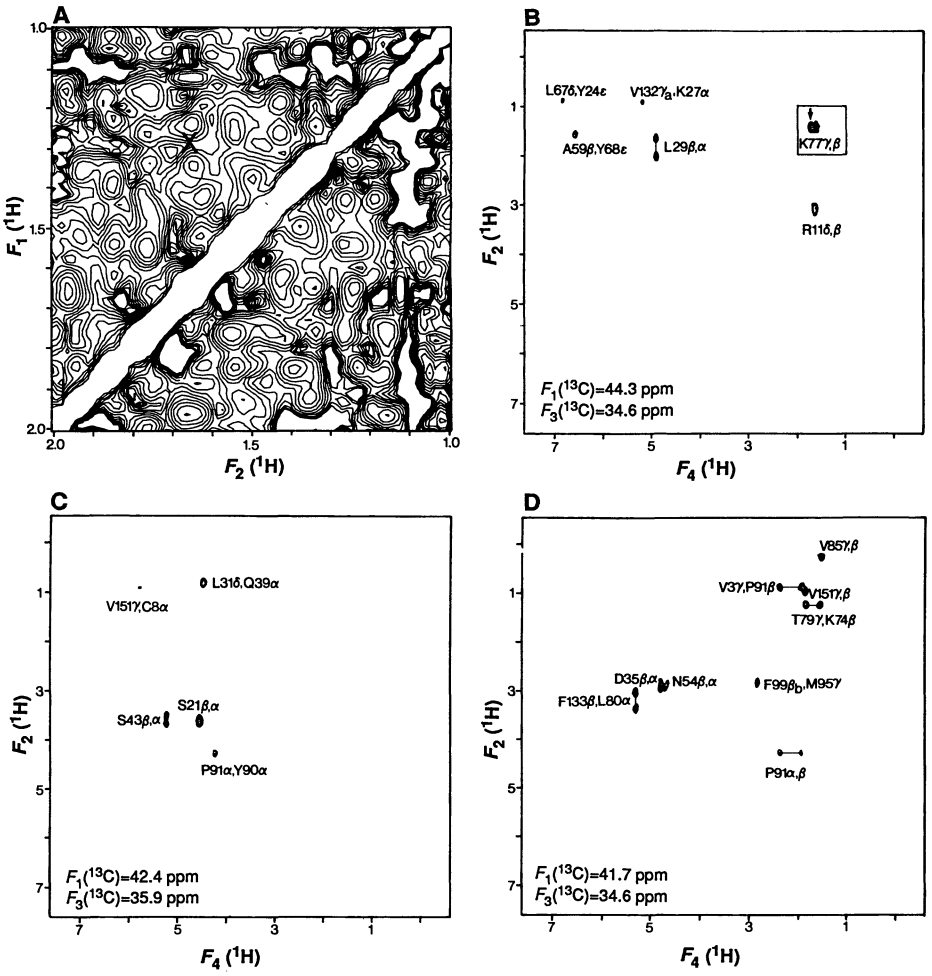

Fig. 6. Comparison of 2D and 4D NMR spectra of IL-1β recorded at 600 MHz (*45*). The region between 1 and 2 ppm of the 2D NOESY spectrum is shown in (**A**). $^1H(F_2)$-$^1H(F_4)$ planes at several $^{13}C(F_1)$ and $^{13}C(F_3)$ frequencies of the 4D ^{13}C-^{13}C NOESY spectrum are shown in (**B**) to (**D**). No individual cross peaks can be observed in the 2D spectrum and the letter X has ^1H coordinates of 1.39 and 1.67 ppm. In contrast, only two cross peaks are observed in the boxed region in (B) between 1 and 2 ppm, one of which (indicated by an arrow) has the same ^1H coordinates as the letter X. Further analysis of the complete 4D spectrum reveals the presence of seven NOE cross peaks superimposed at the ^1H coordinates of the letter X. This can be ascertained by looking at $^{13}C(F_1)$-$^{13}C(F_3)$ plane taken at the ^1H coordinates of X. True diagonal peaks corresponding to magnetization that has not been transferred from one proton to another, as well as intense NOE peaks involving protons attached to the same carbon atom (that is, methylene protons), appear in only a single $^1H(F_2)$-$^1H(F_4)$ plane of each $^{13}C(F_1)$,$^1H(F_2)$,$^1H(F_4)$ cube at the carbon frequency where the originating and destination carbon atoms coincide (that is, at $F_1 = F_3$). Thus, these intense resonances no longer obscure NOEs between proton with similar or degenerate chemical shifts. Two examples of such NOEs can be seen in (C) (between the CαH protons of Pro^{91} and Tyr^{90}) and (D) (between one of the CβH protons of Phe^{77} and the methyl protons of Met^{95}). These various planes of the 4D spectrum also illustrate another key aspect of 3D and 4D NMR, namely, the importance of designing the pulse scheme to optimally remove undesired artifacts that may severely interfere with the interpretation of the spectra (*44*). Thus, although the 4D ^{13}C-^{13}C–edited NOESY experiment is conceptually analogous to that of a 4D ^{13}C-^{15}N–edited one, the design of a suitable pulse scheme is actually much more complex in the ^{13}C-^{13}C case because there are a large number of spurious magnetization transfer pathways that can lead to observable signals in the homonuclear ^{13}C-^{13}C case. For example, in the 4D ^{15}N-^{13}C–edited case there are no "diagonal peaks" that would correspond to magnetization that has not been transferred from one hydrogen to another, as the double heteronuclear filtering (^{13}C and ^{15}N) is extremely efficient at completely removing these normally very intense and uninformative resonances. Such a double filter is not available in the ^{13}C-^{13}C case so that both additional pulses and phase cycling are required to suppress magnetization transfer through these pathways. This task is far from trivial as the number of phase-cycling steps in 4D experiments is severely limited by the need to keep the measurement time down to practical levels (that is, less than 1 week). The results of such care in pulse design can be clearly appreciated from the artifact free planes shown in (B to D). However, when a 4D ^{13}C-^{13}C–edited NOESY spectrum is recorded with the same pulse scheme as that used in the 4D ^{15}N-^{13}C experiment (*44*) (with the obvious replacement of ^{15}N pulses by ^{13}C pulses), a large number of spurious peaks are observed along a pseudo-diagonal at $\delta^1H(F_2) = \delta^1H(F_4)$ in planes where the carbon frequencies of the originating and destination protons do *not* coincide. As a result, it becomes virtually impossible under these circumstances to distinguish artifacts from NOEs between protons with the same ^1H chemical shifts, as was possible with complete confidence in (C) and (D).

IL-1β is shown in Fig. 6A. The overlap is so great that no single individual cross peak can be resolved. One might therefore wonder just how many NOE interactions are actually superimposed, for example, at the ^{1}H chemical shift coordinates of the letter X at 1.39 (F_1) and 1.67 (F_2) ppm. A ^{1}H(F_2)-^{1}H(F_4) plane of the 4D spectrum at δ^{13}C(F_1), δ^{13}C(F_3) = 44.3, 34.6 ppm is shown in Fig. 6B and the square box at the top right-hand side of this panel encloses the region between 1 and 2 ppm. Only two cross peaks are present in this region, and the arrow points to a single NOE between the CγH and CβH protons of Lys^{77} with the same ^{1}H chemical shift coordinates as the letter X in Fig. 6A. All of the other NOE interactions at the same ^{1}H chemical shift coordinates can be determined by inspection of a single ^{13}C(F_1)-^{13}C(F_3) plane taken at δ^1H(F_2),δ^1H(F_4) = 1.39, 1.67 ppm. This spectrum reveals a total of seven NOE interactions superimposed at the ^{1}H chemical shift coordinates of the letter X. Another feature of the 4D spectrum is illustrated by the two ^{1}H(F_2)-^{1}H(F_4) planes at different F_1 and F_3 ^{13}C frequencies shown in Fig. 6, C and D. In both cases, there are cross peaks involving protons with identical or nearly identical chemical shifts, namely that between Pro^{91}(CαH) and Tyr^{90}(CαH), diagnostic of a *cis*-proline, in Fig. 6C, and between Phe^{99}(CβbH) and Met^{95}(CγH) in Fig. 6D. These interactions could not be resolved in either a 2D spectrum or a 3D ^{13}C-edited spectrum as they would lie on the spectral diagonal (that is, the region of the spectrum corresponding to magnetization that has not been transferred from one proton to another). In the 4D spectrum, however, they are easy to observe, provided, of course, that the ^{13}C chemical shifts of the directly bonded ^{13}C nuclei are different.

Because the number of NOE interactions present in each ^{1}H(F_4)-^{1}H(F_2) plane of 4D ^{13}C-^{15}N– or ^{13}C-^{13}C–edited NOESY spectra is so small, the inherent resolution in a 4D spectrum is extremely high, despite the low level of digitization. Indeed, spectra with equivalent resolution can be recorded at magnetic field strengths considerably lower than 600 MHz, although this would obviously lead to a reduction in sensitivity. Further, it can be calculated that 4D spectra with virtual lack of resonance overlap and good sensitivity can be obtained on proteins with as many as 400 residues. Thus, once complete ^{1}H, ^{15}N, and ^{13}C assignments are obtained, analysis of 4D spectra should permit the automated assignment of almost all NOE interactions.

Application of 3D and 4D NMR to Larger Proteins

While the potential of heteronuclear 3D and 4D NMR methods in resolving problems associated with both extensive resonance overlap and large linewidths is obvious, how does this new approach fare in practice? In this regard it should be borne in mind that resonance assignments are only a means to an end, and the true test of multidimensional NMR lies in examining its success in solving the problem that it was originally designed to tackle, namely, the determination of high-resolution 3D structures of larger proteins in solution. This goal has now been attained in the case of IL-1β (17.4 kD), which plays a central role in the immune and inflammatory responses (*10*). This protein is 50% larger than any other protein whose 3D structure has been determined by NMR to date (*29, 32*).

Despite extensive analysis of 2D spectra obtained at different pH

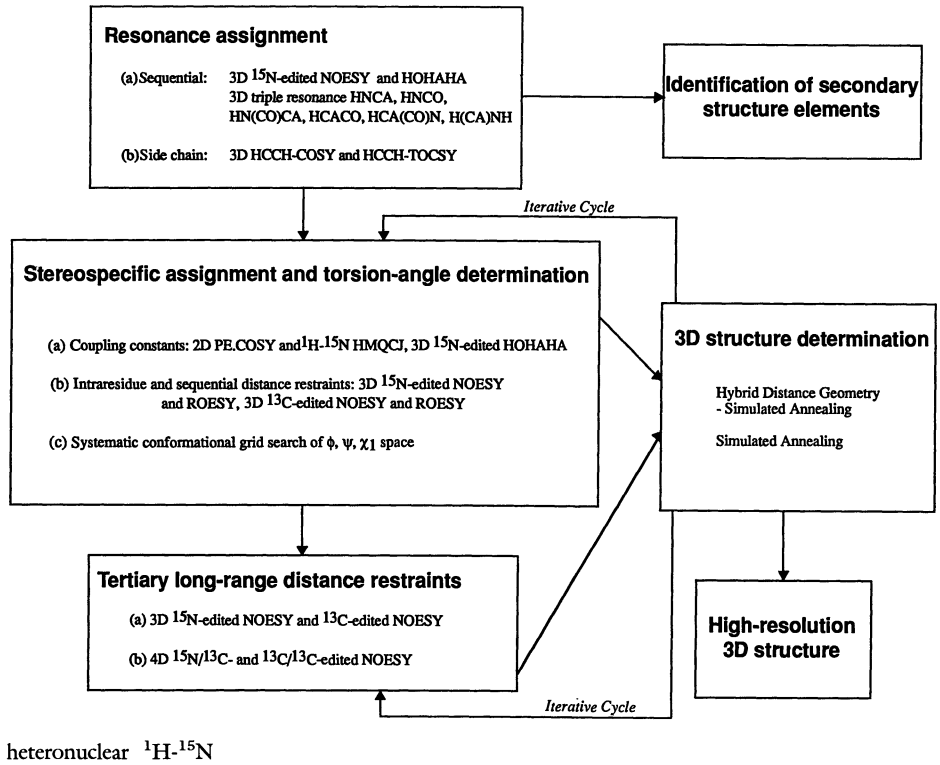

Fig. 7. Outline of the general strategy used in our laboratory to determine the 3D structure of larger proteins such as IL-1β by 3D and 4D NMR. The various NMR experiments are as follows. Through-space interactions are detected in the heteronuclear-edited 3D and 4D NOESY and ROESY experiments (*35, 36, 38, 40, 44–46*). Direct and relayed scalar correlations from the CαH and CβH protons to the NH protons through three-bond ^{1}H-^{1}H couplings are detected in the 3D ^{15}N-edited HOHAHA spectrum (*36–38*); direct and relayed scalar correlations between aliphatic protons through the large $^1J_{CC}$ couplings are observed in the 3D HCCH-COSY and HCCH-TOCSY experiments, respectively (*41–43*). The ^{13}Cα($i-1$,i)-^{15}N(i)-NH(i), ^{13}CO($i-1$)-^{15}N(i)-NH(i) and CαH(i)-^{13}Cα(i)-^{13}CO(i) correlations via direct through-bond connectivities are observed in the 3D HNCA, HNCO, and HCACO experiments, respectively (*48*). Finally, ^{13}Cα($i-1$)-^{15}N(i)-NH(i) and CαH($i-1$)-^{13}Cα($i-1$)-^{15}N(i) correlations via two successive one-bond couplings between the ^{13}Cα($i-1$)-^{13}CO($i-1$) and ^{13}CO($i-1$)-^{15}N(i) atoms are observed in the HN(CO)CA and HCA(CO)N relayed experiments, respectively, while CαH($i-1$,i)-^{15}N(i)-NH(i) correlations can be observed in the H(CA)NH experiment that relays magnetization via the ^{13}Cα atom (*47*). $^3J_{HN\alpha}$ and $^3J_{\alpha\beta}$ ^{1}H-^{1}H coupling constants, which are related to the torsion angles ϕ and χ_1 through empirical Karplus relations (*50*), are measured from 2D heteronuclear ^{1}H-^{15}N HMQC-J (*51*) and homonuclear ^{1}H-^{1}H PE.COSY (*52*) correlation spectra, respectively. A semiquantitative measure of the $^3J_{\alpha\beta}$ couplings, which is sufficient for securing stereospecific assignments and χ_1 torsion angle restraints, can also be obtained from the relative magnitude of the NH-CβH correlations observed in the 3D ^{15}N-edited HOHAHA spectrum (*37*). Stereospecific assignments and torsion-angle restraints are obtained by comparing the relevant experimental data (that is, coupling constants and intraresidue and sequential distance restraints involving the NH, CαH, and CβH protons) to the calculated values of these parameters present in two databases. The first is a systematic one covering the complete ϕ, ψ, and χ_1 conformational space (in a 3D grid spaced at 10° intervals) of a tripeptide fragment with idealized geometry, and the second comprises a library of tripeptide segments from high-resolution x-ray structures (*13*). This procedure is carried out for both possible stereospecific assignments, and when the experimental data are only consistent with one of the two possibilities, the correct stereospecific assignment, as well as allowed ranges for ϕ, ψ, and χ_1, are obtained. The minimum ranges that we use for the torsion angle restraints are ±30°, ±50°, and ±20°, respectively.

values and temperatures, as well as examination of 2D spectra of mutant proteins, it did not prove feasible to obtain unambiguous ^1H assignment for more than ~30% of the residues (*38*). Thus, any further progress could only be made by resorting to higher dimensionality heteronuclear NMR. A summary of the strategy we used for determining its structure is shown in Fig. 7. The initial step involved the complete assignment of the ^1H, ^{15}N, and ^{13}C resonances of the backbone and side chains by using the entire gamut of double and triple resonance 3D experiments listed in the top left-hand panel of Fig. 7 (*38, 43*). In the second step, backbone and side chain torsion angle restraints, as well as stereospecific assignments for β-methylene protons, were obtained by means of a 3D grid search of ϕ,ψ,χ_1 space in which the experimental data for the $^3J_{HN\alpha}$ and $^3J_{\alpha\beta}$ coupling constants and the approximate intraresidue and sequential distance restraints between the NH, CαH, and CβH protons were compared to values present in an extensive database (*13, 14*). In the third step, approximate interproton distance restraints between non-adjacent residues were derived from analysis of 3D and 4D heteronuclear-edited NOESY spectra. Analysis of the 3D heteronuclear-edited NOESY spectra alone was sufficient to derive a low-resolution structure on the basis of a small number of NOEs involving solely NH, CαH, and CβH protons (*49*). However, further progress by using 3D NMR was severely hindered by the numerous ambiguities still present in these spectra, in particular for NOEs arising from the large number of aliphatic protons. Thus, the 4D heteronuclear-edited NOESY spectra proved to be absolutely essential for the successful completion of this task. In addition, the proximity of backbone NH protons to bound structural water molecules was ascertained from a 3D ^{15}N-separated ROESY spectrum that permits one to distinguish specific protein-water NOE interactions from chemical exchange with bulk solvent (*40*). In this regard, we should emphasize again that in our laboratory, all of the NOE data are interpreted in as conservative a manner as possible, and are simply classified into three distance ranges, 1.8 to 2.7 Å, 1.8 to 3.3 Å, and 1.8 to 5.0 Å, which correspond to strong, medium, and weak intensity NOEs, respectively.

With an initial set of experimental restraints in hand, 3D structure calculations were initiated. Typically we use the method of hybrid distance geometry–dynamical simulated annealing in which an approximate polypeptide fold is obtained by projection of a subset of atoms from *n*-dimensional distance space into cartesian coordinate space followed by simulated annealing that includes all of the atoms (*18*). Alternatively we use simulated annealing starting from either random structures with intact covalent geometry or from a completely random array of atoms (*19*). All of these simulated annealing protocols involve solving Newton's equations of motion subject to a simplified target function comprising terms for the experimental restraints, covalent geometry, and nonbonded contacts. The underlying principle consists of raising the temperature of the system and then slowly cooling it in order to overcome false local minima and large potential energy barriers along the path toward the global minimum region of the target function and to sample efficiently and comprehensively the conformational space consistent with the experimental restraints. A key aspect of the overall strategy lies in the use of an iterative approach whereby the experimental data is reexamined in the light of the initial set of calculated structures in order to resolve ambiguities in NOE assignments, to obtain more stereospecific assignments (such as the α-methylene protons of Gly and the methyl groups of Val and Leu) and torsion angle restraints, and to assign backbone hydrogen bonds associated with slowly exchanging NH protons as well as with bound water molecules. The iterative cycle comes to an end when all of the experimental data have been interpreted.

The final experimental data set for IL-1β comprised a total of 3146 approximate and loose experimental restraints made up of 2780 distance and 366 torsion angle restraints (*10*). These data represent an average of ~21 experimental restraints per residue. If one takes into account that interresidue NOEs affect two residues, while intraresidue NOE and torsion angle restraints only affect individual residues, the average number of restraints influencing the conformation of each residue is ~33. A superposition of 32 independently calculated structures is shown in Fig. 8. All 32

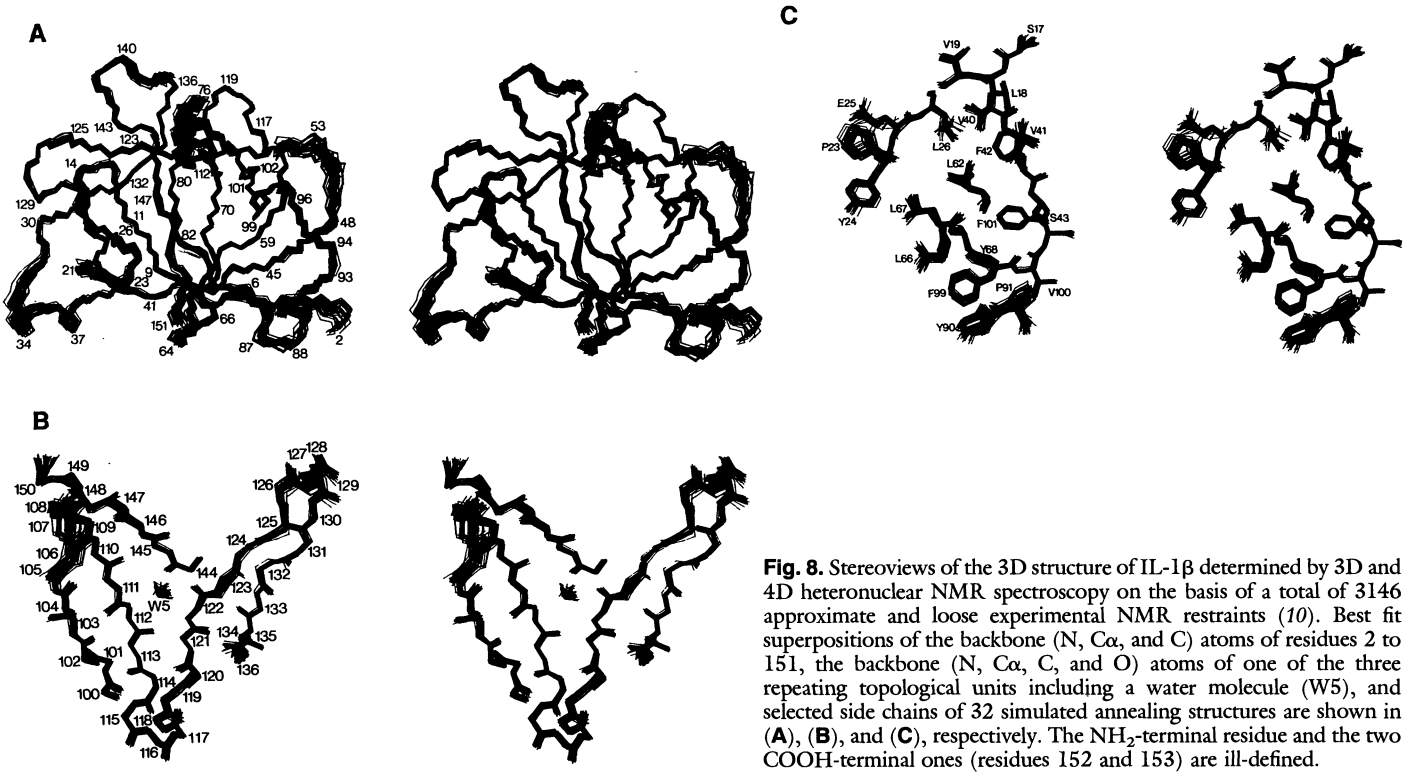

Fig. 8. Stereoviews of the 3D structure of IL-1β determined by 3D and 4D heteronuclear NMR spectroscopy on the basis of a total of 3146 approximate and loose experimental NMR restraints (*10*). Best fit superpositions of the backbone (N, Cα, and C) atoms of residues 2 to 151, the backbone (N, Cα, C, and O) atoms of one of the three repeating topological units including a water molecule (W5), and selected side chains of 32 simulated annealing structures are shown in (**A**), (**B**), and (**C**), respectively. The NH_2-terminal residue and the two COOH-terminal ones (residues 152 and 153) are ill-defined.

structures satisfy the experimental restraints within their specified errors, display very small deviations from idealized covalent geometry, and have good nonbonded contacts. Both the backbone as well as ordered side chains are exceptionally well defined. Indeed, the atomic rms distribution about the mean coordinate positions is 0.4 Å for the backbone atoms, 0.8 Å for all atoms, and 0.5 Å for side chains with ≤40% of their surface (relative to that in a tripeptide Gly-X-Gly) accessible to solvent (*10*).

The structure of IL-1β itself resembles a tetrahedron and displays threefold internal pseudo-symmetry. There are 12 β strands arranged in an exclusively antiparallel β structure, and six of the strands form a β barrel (seen in the front of Fig. 8A) that is closed off at the back of the molecule by the other six strands. Each repeating topological unit is composed of five strands arranged in an antiparallel manner with respect to each other (Fig. 8B). Water molecules occupy similar positions in all three topological units, as well as at the interface of the three units, and are involved in bridging backbone hydrogen bonds. Thus, in the case of the topological unit shown in Fig. 8B, the water molecule labeled W5 accepts a hydrogen bond from the NH of Phe^{112} in strand IX and donates two hydrogen bonds to the backbone carbonyls of Ile^{122} in strand X and Thr^{144} in strand XII. The packing of some internal residues with respect to one another, as well as the excellent definition of internal side chains, is illustrated in Fig. 8C. Because of the high resolution of the IL-1β structure it was possible to analyze in detail side chain–side chain interactions that stabilize the structure. In addition, examination of the structure in the light of mutational data permitted us to propose the presence of three distinct sites involved in the binding of IL-1β to its cell surface receptor (*10*).

Concluding Remarks

In this review we have summarized the recent developments in heteronuclear 3D and 4D NMR that have been designed to extend the NMR methodology to medium-sized proteins in the 15- to 30-kD range. The underlying principle of this approach consists of extending the dimensionality of the spectra to obtain dramatic improvements in spectral resolution while simultaneously exploiting large heteronuclear couplings to circumvent problems associated with larger linewidths. A key feature of all of these experiments is that they do not result in any increase in the number of observed cross peaks relative to their 2D counterparts. Hence, the improvement in resolution is achieved without raising the spectral complexity, which renders data interpretation straightforward. Thus, for example, in 4D heteronuclear-edited NOESY spectra, the NOE interactions between proton pairs are not only labeled by the ^1H chemical shifts but also by the corresponding chemical shifts of their directly bonded heteronuclei in four orthogonal axes of the spectrum. Also important in terms of practical applications is the high sensitivity of these experiments that makes it feasible to obtain high-quality spectra in a relatively short time frame on 1 to 2 mM protein samples uniformly labeled with ^{15}N or ^{13}C or both.

Just as 2D NMR opened the application of NMR to the structure determination of small proteins of less than ~100 residues, 3D and 4D heteronuclear NMR provide the means of extending the methodology to medium-sized proteins in the 150- to 300-residue range. Indeed, the recent determination of the high-resolution structure of IL-1β using 3D and 4D heteronuclear NMR (*10*) demonstrates that the technology is now available for obtaining the structures of such medium-sized proteins at a level of accuracy and precision that is comparable to the best results attainable for small proteins.

REFERENCES AND NOTES

1. Abbreviations: NMR, nuclear magnetic resonance; NOE, nuclear Overhauser enhancement; NOESY, nuclear Overhauser enhancement spectroscopy; ROESY, rotating frame Overhauser spectroscopy; HOHAHA, homonuclear Hartmann-Hahn spectroscopy; TOCSY, total correlation spectroscopy; HMQC, heteronuclear multiple quantum coherence.
2. J. Jeener, paper presented at the Ampere International Summer School, BaskoPolj, Yugoslavia, 1971; W. P. Aue, E. Bartholdi, R. R. Ernst, *J. Chem. Phys.* **64**, 2229 (1976); J. Jeener, B. H. Meier, P. Bachmann, R. R. Ernst, *ibid.* **71**, 4546 (1979).
3. R. R. Ernst, G. Bodenhausen, A. Wokaun, *Principle of Nuclear Magnetic Resonance in One and Two Dimensions* (Clarendon, Oxford, 1987); A. Bax and L. Lerner, *Science* **232**, 960 (1986).
4. M. P. Williamson, T. F. Havel, K. Wüthrich, *J. Mol. Biol.* **182**, 295 (1985).
5. R. Kaptein, E. R. P. Zuiderweg, R. M. Scheek, R. Boelens, W. F. van Gunsteren, *ibid.*, p. 179.
6. G. M. Clore, A. M. Gronenborn, A. T. Brünger, M. Karplus, *ibid.* **186**, 435 (1985).
7. G. M. Clore *et al.*, *EMBO J.* **5**, 2728 (1986).
8. K. Wüthrich, *NMR of Proteins* (Wiley, New York, 1986); G. M. Clore, A. M. Gronenborn, *Protein Eng.* **1**, 275 (1987); R. Kaptein, R. Boelens, R. M. Scheek, W. F. van Gunsteren, *Biochemistry* **27**, 5389; A. Bax, *Annu. Rev. Biochem.* **58**, 223 (1989); J. Markley, *Methods Enzymol.* **176**, 12 (1989); K. Wüthrich, *Science* **243**, 45 (1989); A. M. Gronenborn and G. M. Clore, *Anal. Chem.* **62**, 2 (1990); K. Wüthrich, *J. Biol. Chem.* **265**, 22059 (1990); G. M. Clore and A. M. Gronenborn, *Annu. Rev. Biophys. Biophys. Chem.* **21**, 29 (1991).
9. G. M. Clore and A. M. Gronenborn, *CRC Crit. Rev. Biochem. Mol. Biol.* **24**, 479 (1989).
10. G. M. Clore, P. T. Wingfield, A. M. Gronenborn, *Biochemistry* **30**, 2315 (1991).
11. A. Overhauser, *Phys. Rev.* **89**, 689 (1953); *ibid.* **92**, 411 (1953); I. Solomon, *ibid.* **99**, 559 (1955); J. H. Noggle and R. E. Schirmer, *The Nuclear Overhauser Effect—Chemical Applications* (Academic Press, New York, 1971).
12. G. Wagner *et al.*, *J. Mol. Biol.* **196**, 611 (1987); S. Hyberts, W. Märki, G. Wagner, *Eur. J. Biochem.* **164**, 625 (1987); A. Arseniev *et al.*, *J. Mol. Biol.* **201**, 637 (1988).
13. M. Nilges, G. M. Clore, A. M. Gronenborn, *Biopolymers* **29**, 813 (1990).
14. P. J. Kraulis *et al.*, *Biochemistry* **28**, 7241 (1989).
15. P. Güntert, W. Braun, W. Wider, K. Wüthrich, *J. Am. Chem. Soc.* **111**, 3997 (1989).
16. G. M. Crippen and T. F. Havel, *Acta Crystallogr.* **A34**, 282 (1978); T. F. Havel, I. D. Kuntz, G. M. Crippen, *Bull. Math. Biol.* **45**, 665 (1983); T. F. Havel and K. Wüthrich, *J. Mol. Biol.* **182**, 281 (1985).
17. W. Braun and N. Go, *J. Mol. Biol.* **186**, 611 (1985).
18. M. Nilges, A. M. Gronenborn, G. M. Clore, *FEBS Lett.* **229**, 317 (1988).
19. M. Nilges, A. M. Gronenborn, A. T. Brünger, G. M. Clore, *Protein Eng.* **2**, 27 (1988); M. Nilges, G. M. Clore, A. M. Gronenborn, *FEBS Lett.* **239**, 129 (1988).
20. G. M. Clore, A. T. Brünger, M. Karplus, A. M. Gronenborn, *J. Mol. Biol.* **191**, 523 (1986); A. T. Brünger, G. M. Clore, A. M. Gronenborn, M. Karplus, *Proc. Natl. Acad. Sci. U.S.A.* **83**, 3801 (1986); L. Nilsson, G. M. Clore, A. M. Gronenborn, A. T. Brünger, M. Karplus, *J. Mol. Biol.* **188**, 455 (1986); A. M. Gronenborn and G. M. Clore, *Biochemistry* **28**, 5978 (1989).
21. W. Braun, *Q. Rev. Biophys.* **19**, 115 (1987); G. M. Crippen and T. F. Havel, *Distance Geometry and Molecular Conformation* (Wiley, New York, 1988); G. M. Clore, M. Nilges, A. M. Gronenborn, in *Computer-Aided Molecular Design*, W. G. Richards, Ed. (IBC Technical Services, London, 1989), pp. 203–219; I. D. Kuntz, J. F. Thomason, C. M. Oshiro, *Methods Enzymol.* **177**, 159 (1989); R. M. Scheek, W. F. van Gunsteren, R. Kaptein, *ibid.*, p. 204; G. M. Clore and A. M. Gronenborn, in *Proteins*, vol. 2 of *Theoretical Biochemistry and Molecular Biophysics*, D. L. Beveridge and R. Lavery, Eds. (Adenine, New York, 1991), pp. 1–16.
22. P. C. Driscoll, A. M. Gronenborn, G. M. Clore, *FEBS Lett.* **243**, 223 (1989).
23. P. C. Driscoll, A. M. Gronenborn, L. Beress, G. M. Clore, *Biochemistry* **28**, 2188 (1989).
24. G. M. Clore, E. Appella, M. Yamada, K. Matsushima, A. M. Gronenborn, *ibid.* **29**, 1689 (1989).
25. V. Luzzati, *Acta Crystallogr.* **5**, 802 (1952); C. Chothia and A. Lesk, *EMBO J.* **5**, 823 (1986); J. Kuryan, G. A. Petzko, R. Levy, M. Karplus, *J. Mol. Biol.* **190**, 227 (1986); T. L. Blundell, B. L. Sibanda, M. J. E. Sternberg, J. M. Thornton, *Nature* **326**, 347 (1987); A. T. Brünger, *J. Mol. Biol.* **203**, 803 (1988); in *Molecular Dynamics: Applications to Molecular Biology*, J. M. Goodfellow, Ed. (Macmillan, London, 1991), pp. 137–178; *Annu. Rev. Phys. Chem.* **42**, 197 (1991); G. M. Clore and A. M. Gronenborn, *J. Mol. Biol.*, in press.
26. E. T. Baldwin *et al.*, *Proc. Natl. Acad. Sci. U.S.A.* **88**, 502 (1991).
27. A. D. Kline, W. Braun, K. Wüthrich, *J. Mol. Biol.* **204**, 675 (1988).
28. P. J. M. Folkers *et al.*, *Biochemistry* **28**, 2601 (1989); H. Haruyama and K. Wüthrich, *ibid.*, p. 4301.
29. H. J. Dyson, G. P. Gippert, D. A. Case, A. Holmgren, P. E. Wright, *ibid.* **29**, 4129 (1990).
30. Y. Q. Qian *et al.*, *Cell* **59**, 573 (1989); M. Billeter *et al.*, *J. Mol. Biol.* **214**, 183 (1990).
31. J. G. Omichinski, G. M. Clore, E. Appella, K. Sakaguchi, A. M. Gronenborn, *Biochemistry* **29**, 9324 (1989).
32. J. D. Forman-Kay, G. M. Clore, P. T. Wingfield, A. M. Gronenborn, *ibid.* **30**, 2685 (1991).
33. C. Griesinger, O. W. Sørensen, R. R. Ernst, *J. Magn. Reson.* **73**, 574 (1987).
34. H. Oschkinat *et al.*, *Nature* **332**, 374 (1988).
35. S. W. Fesik and E. R. P. Zuiderweg, *J. Magn. Reson.* **78**, 588 (1988); D. Marion, L. E. Kay, S. W. Sparks, D. A. Torchia, A. Bax, *J. Am. Chem. Soc.* **111**, 1515

(1989); L. E. Kay, D. Marion, A. Bax, *J. Magn. Reson.* **84**, 72 (1989); E. R. P. Zuiderweg and S. W. Fesik, *Biochemistry* **28**, 2387 (1989); B. A. Messerle, G. Wider, G. Otting, C. Weber, K. Wüthrich, *J. Magn. Reson.* **85**, 608 (1989); M. Ikura, A. Bax, G. M. Clore, A. M. Gronenborn, *J. Am. Chem. Soc.* **112**, 9020 (1990); T. Frenkiel, C. Bauer, M. D. Carr, B. Birdsall, J. Feeney, *J. Magn. Reson.* **90**, 420 (1990).
36. D. Marion *et al.*, *Biochemistry* **29**, 6150 (1989).
37. G. M. Clore, A. Bax, A. M. Gronenborn, *J. Biomol. NMR*, in press.
38. P. C. Driscoll, G. M. Clore, D. Marion, P. T. Wingfield, A. M. Gronenborn, *Biochemistry* **29**, 3542 (1990); P. C. Driscoll, A. M. Gronenborn, P. T. Wingfield, G. M. Clore, *ibid.*, p. 4468.
39. M. Ikura, L. E. Kay, R. Tschudin, A. Bax, *J. Magn. Reson.* **86**, 204 (1990); E. R. P. Zuiderweg, L. P. McIntosh, F. W. Dahlquist, S. W. Fesik, *ibid.*, p. 210.
40. G. M. Clore, A. Bax, P. T. Wingfield, A. M. Gronenborn, *Biochemistry* **29**, 5671 (1990).
41. A. Bax *et al.*, *J. Magn. Reson.* **87**, 620 (1990); L. E. Kay and M. Ikura, A. Bax, *J. Am. Chem. Soc.* **112**, 888 (1990).
42. A. Bax, G. M. Clore, A. M. Gronenborn, *J. Magn. Reson.* **88**, 425 (1990).
43. G. M. Clore, A. Bax, P. C. Driscoll, P. T. Wingfield, A. M. Gronenborn, *Biochemistry* **29**, 8172 (1990).
44. L. E. Kay, G. M. Clore, A. Bax, A. M. Gronenborn, *Science* **249**, 411 (1990).
45. G. M. Clore, L. E. Kay, A. Bax, A. M. Gronenborn, *Biochemistry* **30**, 12 (1991).
46. E. R. P. Zuiderweg, A. M. Petros, S. W. Fesik, E. T. Olejniczak, *J. Am. Chem. Soc.* **113**, 370 (1991).
47. S. W. Fesik *et al.*, *ibid.* **112**, 886 (1990).
48. M. Ikura, L. E. Kay, A. Bax, *Biochemistry* **29**, 4659 (1990); L. E. Kay, M. Ikura, R. Tschudin, A. Bax, *J. Magn. Reson.* **89**, 496 (1990); L. E. Kay, M. Ikura, A. Bax, *ibid.* **91**, 84 (1991); M. Ikura and A. Bax, *J. Biomol. NMR*, in press; R. Powers, A. M. Gronenborn, A. Bax, *J. Magn. Reson.*, in press.
49. G. M. Clore, P. C. Driscoll, P. T. Wingfield, A. M. Gronenborn, *J. Mol. Biol.* **214**, 811 (1990).
50. M. Karplus, *J. Am. Chem. Soc.* **85**, 2870 (1963); A. DeMarco, M. Llina, K. Wüthrich, *Biopolymers* **17**, 617 (1978); A. Pardi, M. Billeter, K. Wüthrich, *J. Mol. Biol.* **180**, 741 (1984).
51. L. E. Kay and A. Bax, *J. Magn. Reson.* **86**, 110 (1990); A. M. Gronenborn, A. Bax, P. T. Wingfield, G. M. Clore, *FEBS Lett.* **243**, 93 (1989); J. D. Forman-Kay, A. M. Gronenborn, L. E. Kay, P. T. Wingfield, G. M. Clore, *Biochemistry* **29**, 1566 (1990).
52. L. Mueller, *J. Magn. Reson.* **72**, 191 (1987); A. Bax and L. E. Lerner, *ibid.* **79**, 429 (1988); D. Marion and A. Bax, *ibid.* **80**, 528 (1988).
53. We thank our many colleagues, past and present, who have contributed to the work carried out in our laboratory. Above all others, we thank A. Bax, with whom we have shared numerous stimulating discussions, fruitful experiments, and a continuous and most enjoyable collaboration in the best of scientific spirits. In addition, we thank W. Eaton and A. Szabo for many constructive and helpful comments during the preparation of this manuscript. The work in the authors' laboratory was supported in part by the AIDS Targeted Anti-Viral Program of the Office of the Director of the National Institutes of Health.

Research Article

Asteroid 1986 DA: Radar Evidence for a Metallic Composition

S. J. OSTRO, D. B. CAMPBELL, J. F. CHANDLER, A. A. HINE, R. S. HUDSON, K. D. ROSEMA, I. I. SHAPIRO

Echoes from the near-Earth object 1986 DA show it to be significantly more reflective than other radar-detected asteroids. This result supports the hypothesis that 1986 DA is a piece of NiFe metal derived from the interior of a much larger object that melted, differentiated, cooled, and subsequently was disrupted in a catastrophic collision. This 2-kilometer asteroid, which appears smooth at centimeter to meter scales but extremely irregular at 10- to 100-meter scales, might be (or have been a part of) the parent body of some iron meteorites.

NEAR-EARTH ASTEROIDS, LIKE METEORITES, ARE THOUGHT to come primarily from mainbelt asteroids (*1, 2*). The relations among meteorites, near-Earth asteroids (NEAs), mainbelt asteroids (MBAs), and comets are central to our understanding of conditions in the primitive solar nebula, planetary formation, the collisional evolution of the asteroid belt, and the delivery of small bodies into Earth-crossing orbits. As compositions of asteroids bear directly on these issues, much astronomical effort is devoted to obtaining and interpreting information about asteroid mineralogy. Many NEAs and MBAs have been classified on the basis of their photometric colors and albedos. Visible-infrared (VIS-IR) reflectance spectra have established important mineralogical characteristics that limit the set of plausible meteorite analogs for the most populous classes (*3–7*). For example, C asteroids contain hydrated silicates, carbon, organics, and opaques and are analogous to CI1 and CM2 carbonaceous chondrites. The S asteroids contain pyroxene, olivine, and NiFe metal, and probably correspond to stony iron meteorites or ordinary chondrites or both. The M asteroids contain NiFe metal or assemblages of enstatite and NiFe metal or a combination of both, and probably correspond to iron meteorites or enstatite chondrites or both.

Iron and stony iron meteorites are igneous assemblages derived from differentiated parent bodies, whereas chondrites are relatively primitive, undifferentiated assemblages, so the different candidate meteoritic analogs to the M and S classes have disparate cosmogonic implications. Radar observations can probe asteroid-meteorite relations because metal concentration influences radar reflectivity dramatically and iron and stony iron meteorites are much more metallic than chondrites. Only two M NEAs, 1986 DA and 3554 Amun (1986 EB), have been identified (*8, 9*). We report radar observations of 1986 DA that constrain this object's physical properties, and we argue that it is mineralogically similar to iron meteorites.

S. J. Ostro and K. D. Rosema are at the Jet Propulsion Laboratory, California Institute of Technology, Pasadena, CA 91109. D. B. Campbell is at the National Astronomy and Ionosphere Center, Cornell University, Ithaca, NY 14853. J. F. Chandler and I. I. Shapiro are at the Harvard-Smithsonian Center for Astrophysics, Cambridge, MA 02138. A. A. Hine is at the National Astronomy and Ionosphere Center, Box 995, Arecibo, PR 00613. R. S. Hudson is in the Electrical and Computer Engineering Department, Washington State University, Pullman, WA 99164.